Collective excitations in the tetravalent lanthanide honeycomb antiferromagnet, Na_2PrO_3

M. J. Daum,[1,*] A. Ramanathan,[2,*] A. I. Kolesnikov,[3] S. A. Calder,[3] M. Mourigal,[1,†] and H. S. La Pierre[2,4,‡]

[1] *School of Physics, Georgia Institute of Technology, Atlanta, GA 30332, USA*
[2] *School of Chemistry and Biochemistry, Georgia Institute of Technology, Atlanta, GA 30332, USA*
[3] *Neutron Scattering Division, Oak Ridge National Laboratory, Oak Ridge, TN 37831, USA*
[4] *Nuclear and Radiological Engineering and Medical Physics Program, School of Mechanical Engineering, Georgia Institute of Technology, Atlanta, GA 30332, USA*

(Dated: October 13, 2020)

Thermomagnetic and inelastic neutron scattering measurements on Na_2PrO_3 are reported. This material is an antiferromagnetic honeycomb magnet based on the tetravalent lanthanide Pr^{4+} and has been proposed to host dominant antiferromagnetic Kitaev interactions. These measurements reveal magnetic fluctuations in Na_2PrO_3 below an energy of 2 meV as well as crystal-field excitations around 230 meV. The latter energy is comparable to the scale of the spin-orbit interaction and explains both the very small effective moment of around 1.0 μ_B per Pr^{4+} and the difficulty to uncover any static magnetic scattering below the ordering transition at $T_N = 4.6$ K. By comparing the low-energy magnetic excitations in Na_2PrO_3 to that of the isostructural spin-only compound, Na_2TbO_3, a microscopic model of exchange interactions is developed that implicates dominant and surprisingly large Heisenberg exchange interactions $J \approx 1.1(1)$ meV. Although antiferromagnetic Kitaev interactions with $K \leq 0.2J$ cannot be excluded, the inelastic neutron scattering data of Na_2PrO_3 is best explained with a $\Delta = 1.24(2)$ easy-axis XXZ exchange anisotropy.

Frustrated quantum magnets have been proposed as a platform to realize quantum spin-liquids (QSLs) and other exotic forms of magnetic matter [1, 2]. In QSLs, quantum fluctuations are so strong that spins remain disordered for temperatures well below the average interaction scale between spins and become entangled. Geometrically frustrated lattices featuring lanthanide ions have gained much recent attention, including the triangular, kagome, and pyrochlore systems [3–8]. An alternative realization of a QSL (with an exact solution) was proposed by Kitaev based on $S = 1/2$ moments on a honeycomb lattice with bond-dependent Ising-like interactions [9]. While the honeycomb lattice is not inherently frustrated, anisotropic interactions, parametrized by the Kitaev term (K), give rise to frustration between the competing orthogonal anisotropy axes. However, in real materials, the Kitaev interactions are often perturbed by Heisenberg interactions (J) giving rise to the strongly frustrated Heisenberg-Kitaev (J–K) model [10, 11].

Bond-dependent interactions stem from strong spin-orbit coupling in magnetic insulators. Hence heavy $4d$ and $5d$ transition metal ions have been proposed as a paradigm to realize a Kitaev QSL [12, 13]. Spin-orbit $J_{\text{eff}} = 1/2$ Mott insulators comprising low-spin d^5 and d^7 transition metal ions, such as Na_2IrO_3, $H_3LiIr_2O_6$, Li_2IrO_3, and $RuCl_3$ have been extensively studied to search for Kitaev physics [14–20]. An alternative approach is to explore $J_{\text{eff}} = 1/2$ magnetic moments from f-element ions, which exhibit significant anisotropy [21, 22]. In the $4f$ electron manifold, several electron configurations can host $J_{\text{eff}} = 1/2$ magnetic moments, with the one electron/one-hole ($4f^1/4f^{13}$) configurations as the most desirable. The one hole case is realized by the $J_{\text{eff}} = 1/2$ honeycomb material $YbCl_3$, the collective behavior of which was recently shown to be best described from the Heisenberg limit [23]. The one electron case leads to the $4f^1$ ions Ce^{3+} or Pr^{4+} including Na_2PrO_3, a material with edge sharing PrO_6 octahedra forming a honeycomb network similar to the iridates and recently proposed to exhibit dominant antiferromagnetic Kitaev interactions, contrasting with $4d$ and $5d$ systems [24].

In this work, the magnetic properties of Na_2PrO_3 are investigated using a combination of thermomagnetic and neutron scattering measurements on powder samples. These studies uncover spin-wave-like excitations at energies below 2 meV. A comparison to the isostructural compounds Na_2TbO_3 and Na_2CeO_3, that represent spin-only magnetic-moment and non-magnetic analogues of the title compound, respectively, yield deeper insights into the effective magnetic Hamiltonian of Na_2PrO_3. Although no magnetic Bragg peaks are observed within experimental sensitivity below the $T_N \approx 4.6$ K transition seen in thermomagnetic probes, dynamic correlations in Na_2PrO_3 are well explained by a model including antiferromagnetic nearest-neighbor interactions and a easy-axis XXZ exchange anisotropy. The inelastic data does not support the presence of a sizeable Kitaev term K. These studies also reveal an unusually small effective magnetic moment for the Pr^{4+} ions which is explained by the increased crystal-field splitting in comparison to trivalent lanthanides [25, 26].

Polycrystalline samples of $Na_2Ln^{4+}O_3$ with Ln = Ce ($4f^0$), Pr ($4f^1$), Tb ($4f^7$) were synthesized by solid-state reactions and structurally characterized by synchrotron x-ray diffraction [see Supplementary Information (SI) Sec. S1]. Na_2PrO_3 contains layers of PrO_6 octa-

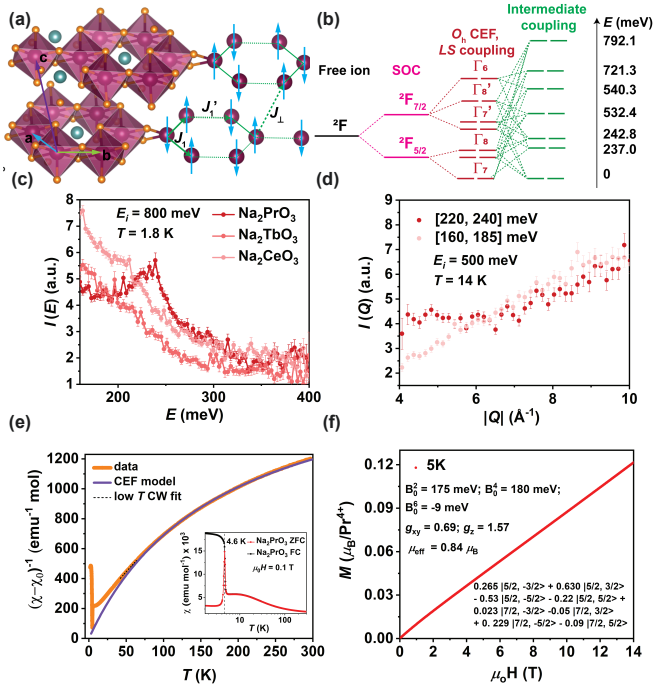

FIG. 1. (a) Monoclinic crystal structure of Na_2PrO_3 showing the honeycomb layers of Pr^{4+} ions and the resulting nearest neighbor and out-of-plane magnetic exchange pathways. (b) Comparison of the expected splitting of the $^2F_{5/2}$ free-ion ground-state of Pr^{4+} by SOC and a O_h CEF environment in LS and intermediate coupling. (c) Comparison between low momentum-transfer $Q \leq 6$ Å^{-1} inelastic neutron scattering spectra measured with $E_i = 800$ meV for Na_2LnO_3 (Ln = Ce, Pr, Tb) at $T = 1.8$ K. (d) Momentum-transfer dependence of the $E = 233(1)$ meV excitation at $T = 14$ K compared to phonon background at comparable energies. (e) The inverse magnetic susceptibility $1/(\chi(T) - \chi_0)$ and susceptibility $\chi(T)$ of Na_2PrO_3 in a 0.1 T field and $\chi_0 = 1.09 \times 10^{-3}$ emu mole^{-1}. The bold solid line (purple) is the CEF comparison to the data with the parameters of panel (f). The black and red traces in the inset corresponds to field-cooled (FC) and zero-field cooled measurements, respectively. (f) Isothermal magnetization $M(H)$ at $T = 5$ K and obtained CEF parameters.

hedra forming distorted honeycomb networks separated by layers of Na ions, with two intraplane Pr–Pr distances $d = 3.407(3)$ Å and $d' = 3.487(6)$ Å, and an inter-plane distance of $d_\perp \approx 5.8$ Å at $T = 100$ K [Fig. 1(a)]. The ABC stacking sequence in the $C2/c$ space group originates from symmetry breaking displacements of the Na atoms which also lead to evident stacking faults in diffraction patterns. Na_2CeO_3 and Na_2TbO_3 are isostructural to Na_2PrO_3 [27] [see SI Sec. S1]. Given the air-sensitivity of these samples, all synthesis and measurement operations where performed in an inert-gas atmosphere.

To understand the single-ion properties of Na_2PrO_3, broadband inelastic neutron scattering measurements on the fine-resolution Fermi chopper spectrometer (SEQUOIA) [28, 29] were performed at the Spallation Neutron Source (SNS), Oak Ridge National Laboratory (ORNL). Experiments were performed on ($m = 8$ g) polycrystalline samples loaded in annular Al powder cans and inserted into a liquid ^{4}He cryostat reaching a base temperature of $T = 1.5$ K. The data was reduced in MANTID [30] to yield the neutron scattering intensity $I(Q, E)$ as a function of momentum-transfer Q and energy-transfer E. We used a series of incoming energies to probe possible crystal electric field (CEF) excitations of our samples up to an energy transfer of $E \approx 500$ meV [see SI Sec. S2].

Pr^{4+} is a $4f^1$ Kramers ion, isoelectronic to Ce^{3+}, with a $^2F_{5/2}$ free-ion ground-state. For an octahedral oxygen environment with O_h symmetry, the CEF splitting leads to a Kramers doublet ground-state (Γ_7) and an excited quartet (Γ_8) which we expect to split into two doublets given the lower D_{2d} site-symmetry of Pr^{4+} in Na_2PrO_3 [Fig. 1(b)]. The energy-dependence of the neutron scattering intensity at low momentum-transfer $I(Q \leq 6$ Å$^{-1}, E)$ was used to search for these CEF excitations. The comparison of different E_i's and samples [Fig. 1(c) and SI Sec. S2] reveals a strong excitation at $E = 233(1)$ meV. The intensity of the excitation increases at low Q as expected for magnetic scattering [Fig. 1(d)]. The excitation found in Na_2PrO_3 compares well to the 260 meV Γ_7 to Γ_8 splitting observed for $BaPrO_3$ [31] which comprises Pr^{4+} ions in an ideal O_h environment. Since no other CEF excitations are observed below 500 meV, the $E = 233$ meV mode is associated with the two quasi-degenerate Γ_8 doublets [See SI Sec. S2].

Given this quasi-degeneracy, the CEF Hamiltonian can be written using the Wybourne tensor operators as $\hat{\mathcal{H}}_{\rm CEF} = B_0^2\hat{C}_0^2 + B_0^4(\hat{C}_0^4 + 5\hat{C}_4^4) + B_0^6(\hat{C}_0^6 - 21\hat{C}_4^6)$ where the B_0^2 parameter reflects the small axial distortion of the PrO_6 octahedral away from O_h [See SI Sec. S3]. The large CEF energy scale in Na_2PrO_3 has been observed indirectly by O K-edge X-ray absorption near edge spectroscopy studies of PrO_2 [26], and is similar in magnitude to the spin-orbit interaction $\lambda \approx 100$ meV resulting in a ≈ 360 meV separation between $^2F_{5/2}$ and $^2F_{7/2}$ for a free Pr^{4+} ion [32, 33]. As a result, a mixing of the $^2F_{5/2}$ and $^2F_{7/2}$ electronic manifolds is expected and the above Hamiltonian must be diagonalized using the complete set of intermediate-coupling basis states using SPECTRE [34].

The three CEF parameters are constrained by the observed excitation and further determined by matching the calculated temperature-dependence of the magnetic susceptibility to our measurements for $\mu_0 H = 0.1$ T [Fig. 1(e)]. An excellent agreement is obtained for $T \geq 60$ K for the CEF parameters of Fig. 1(f) and a temperature independent term χ_0 is determined to be 1.09×10^{-3} emu.mol^{-1}. The value of χ_0 is in reasonable agreement with the estimated value [35] $\chi_0 \approx \frac{8}{3\lambda}\mu_B^2 N_A = 0.8 \times 10^{-3}$ emu.mol^{-1} for a Pr^{4+} ion and with observations for the related compound $BaPrO_3$ [36]. This result indicates a ground-state doublet dominated by $|^2F_{5/2}, \pm 3/2\rangle$ and

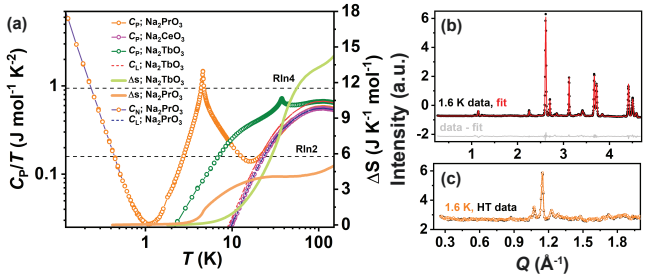

FIG. 2. (a) Heat capacity measurments of our $Na_2Ln^{4+}O_3$ samples measured using the relaxation method above T = 2 K. For Na_2PrO_3, measurements down to $T = 100$ mK were carried out using a dilution refrigerator insert on pressed pellets mixed with Ag. The change in magnetic entropy for Na_2PrO_3 and Na_2TbO_3 is obtained after subtracting the (scaled) lattice contribution from Na_2CeO_3. (b) Neutron diffration measurements on Na_2PrO_3 at T = 1.6 K using λ = 2.4 Å. The red line is the result from a Rietveld refinement. (Inset) Comparison at low-angle diffraction between $T = 1.6$ K and $T = 20$ K.

$|^2F_{7/2}, \pm 5/2\rangle$ states and predicts several higher-energy doublets beyond the 500 meV reach of our experiments [see SI Sec. S3]. This fit also yields a calculated powder-averaged $g = 0.98$ for effective $J_{\rm eff} = 1/2$. The effective moment $\mu^{\rm eff}_{\rm CEF} = 0.84\ \mu_{\rm B}$/Pr is unusually small given the free-ion value is $\mu^{\rm free}_{\rm eff} = 2.54\mu_{\rm B}$/Pr. The small g-tensor is evident from the experimental isothermal magnetization at $T = 5$ K, which is linear and reaches only $\approx 0.12\ \mu_{\rm B}$/Pr at $\mu_0 H = 14$ T, far short of saturation [Fig. 1(f)].

Below $T \approx 40$ K, the susceptibility of Na_2PrO_3 deviates from the single-ion form and culminates in a magnetic transition at $T_N = 4.6$ K, consistent with Ref. 37, with a clear splitting between field-cooled (FC) and zero-field cooled (ZFC) traces but no visible frequency dependence in ac susceptibility [See SI Sec. S4]. Thus, this sharp peak is interpreted as magnetic ordering preceded by short-range order [Fig. 1(e)]. It is difficult to find an adequate regime for a Curie-Weiss analysis: a fit limited to $40 \le T \le 60$ K yields an antiferromagnetic Weiss constant $\Theta_{\rm W} = -30.4(1)$ K and $\mu^{\rm eff}_{\rm CW} = 1.19(1)\mu_{\rm B}$/Pr, comparable to $\mu^{\rm eff}_{\rm CEF}$. Heat capacity measurements [See SI Sec. S5] corroborate this picture [Fig. 2(a)]. An additional upturn is observed below $T = 0.3$ K, which is associated with nuclear spins. Subtracting the lattice contribution reveals an entropy change $\Delta S \approx 0.76R \ln 2$ between 0.1 K and 40 K, corroborating the $J_{\rm eff} = 1/2$ picture for Pr^{4+} and revealing some missing entropy.

To understand the ground-state of Na_2PrO_3 below the transition, neutron powder diffraction experiments were performed on the HB2A diffractometer [38] at the High Flux Isotope Reactor (HFIR), ORNL. No additional Bragg peaks are observed beyond the $C2/c$ nuclear structure [Fig. 2(b)], even after subtracting a $T = 55$ K background [Fig. 2(b)-inset]. Given the high incoherent scattering background from the sample [See SI Sec. S2], the small effective moment of Pr^{4+}, the stacking faults in the crystal structure, and the likelihood of a $\boldsymbol{k}_{\rm m} = 0$ propagation vector, this result is not entirely surprising. To get an estimate on any ordered moment $\langle \mu^z \rangle$, the hyperfine coupling in the nuclear specific-heat was modeled using a Schottky form. Assuming the entire upturn is nuclear yields a static electronic moment $\langle \mu^z_{\rm hyp} \rangle = 0.41\mu_{\rm B}$ at the time-scale of the nuclear-lattice relaxation [39], which is comparable to $\langle \mu^z_{\rm CEF} \rangle = 0.49\ \mu_{\rm B}$ estimated from CEF calculations.

In the absence of visible magnetic Bragg peaks in Na_2PrO_3, low-energy inelastic neutron scattering ($E_i = 8$, 20 meV) was employed to search for magnetic fluctuations. It is instructive to compare these results to the isostructural spin-only compound, Na_2TbO_3 [Fig. 3(a–e)]. Na_2TbO_3 orders at $T'_{\rm N} = 38.2$ K and develops structured spin-wave excitations below $T'_{\rm N}$ [Fig. 3(a,b)] with a band-top of 5 meV and a ≈ 1 meV gap. Inspecting the elastic line, and subtracting $T = 55$ K data from $T = 10$ K, evidences intense magnetic Bragg peaks indexed by a $\boldsymbol{k}_{\rm m} = 0$ propagation vector [Fig. 3(d)]. Representation analysis in SARAH [40] yields four possible magnetic structures, only one of which yields a good fit following a Rietveld refinement in FULLPROF [41] [See SI Sec. S6]. Spins in the resulting Néel ordered structure [Fig. 3(d)-inset] lie in the ac-plane, essentially along c. Spin-wave excitations in Na_2TbO_3 are very intense given $S = 7/2$ and can be efficiently modeled using linear spin-wave theory [42] in SPINW [43]. A spin Hamiltonian $\mathcal{H} = \mathcal{H}_{\rm ex} + D\sum_i (S^z_i)^2$ with Heisenberg exchange interactions J_1 and J'_1 for the split nearest-neighbor pairs (d and d'), $J_\perp$ between inequivalent lanthanide sites in two adjacent honeycomb planes, and a single-ion anisotropy term D is considered. The calculated powder-averaged intensity is in excellent agreement with the data [Fig. 3(c)] with parameters obtained after a grid-calculation and subsequent search for a minimal χ^2 [See SI Sec. S7]. These parameters, $J_1 = 0.50$ meV, $J'_1 = 0.85J_1$, $J_\perp = -0.02J_1$ and $D = -0.001J_1$, indicate that the observed band-top dispersion [Fig. 3(a,b)] is induced by the splitting of J_1 and J'_1, and that the small spin gap is the combined effect of ferromagnetic $J_\perp$ and easy-axis D.

This forgoing analysis facilitates the description of the magnetic fluctuations in Na_2PrO_3 at $T = 1.5$ K [Fig. 3(f–i)], which resemble the spin-wave excitations in Na_2TbO_3 [Fig. 3(a)], but with a reduced band-top of 2 meV [Fig. 3(f)] and a ten-fold decrease in scattering intensity. Thus, a high temperature subtraction ($T = 55$ K) was utilized [Fig. 3(f)]. Given that no static magnetic scattering is observed, an incipient $\boldsymbol{k}_{\rm m} = 0$ order is assumed by analogy with Na_2TbO_3. Given the $J_{\rm eff} = 1/2$ magnetic moments, several models are adopted to incorporate exchange anisotropies (scaled to the corresponding primary exchange) on J_1 and J'_1 bonds, with spin-wave theory calculations performed in SPINW [See SI Sec. S8]. Including a diagonal exchange anisotropy (XXZ), *e.g.*

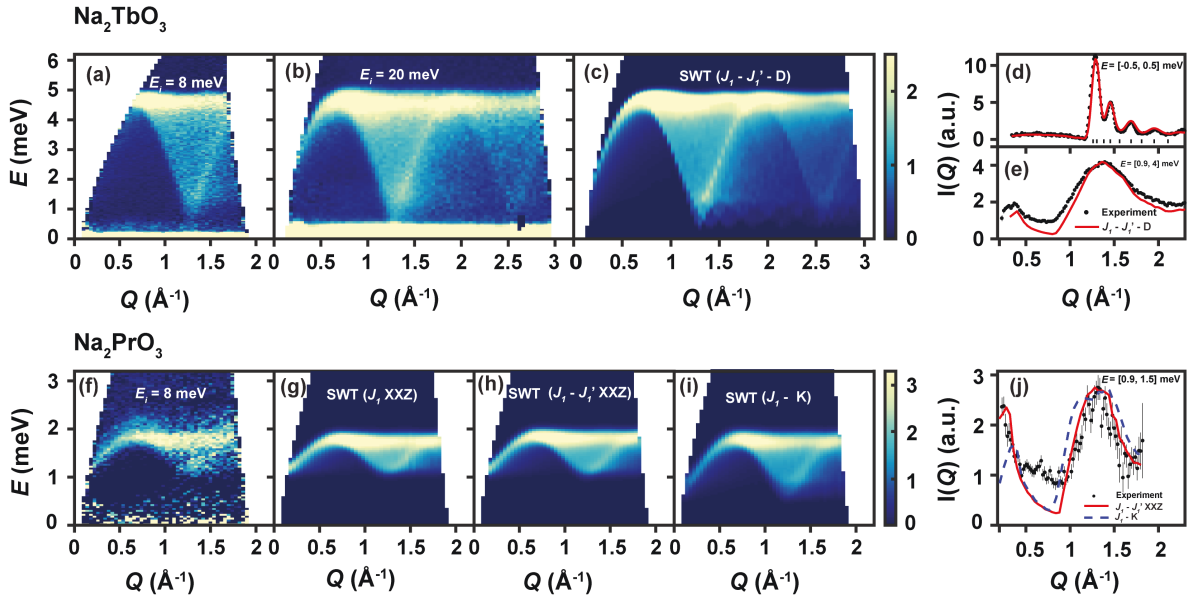

FIG. 3. (a-e) Inelastic neutron scattering intensity $I(Q, E)$ from Na_2TbO_3 at $T = 1.5$ K using (a) $E_i = 8$ meV or (b) $E_i = 20$ meV. (c) Comparison with powder-averaged linear spin-wave theory calculations for optimized parameters including the magnetic form factor of Tb^{3+} and a constant energy energy broadening factor of 0.2 meV. (d) Elastic magnetic scattering $-0.5 \leq E \leq 0.5$ meV of Na_2TbO_3 obtained by subtracting $T = 20$ K data from $T = 55$ K (black dots). The red line and vertical black ticks are the result of a Rietveld refinement using a $\boldsymbol{k}_m = 0$ propagation vector. (e) Momentum dependence of the low-energy inelastic signal $0.9 \leq E \leq 4$ meV (black dots) and comparison to linear spin-wave-theory predictions for optimized parameters (red line). (f-j) Inelastic neutron scattering results from Na_2PrO_3 at $T = 1.5$ K using (f) $E_i = 8$ meV and $T = 55$ K subtracted. Comparison to linear spin-wave-theory predictions with optimized parameters for (g) a J_1 XXZ model with $\Delta = 1.22$ ($J_1 = 1.06$ meV), (h) a J_1–J_1' XXZ model with $\Delta = 1.26$ and $J_1' = 0.85J_1$ ($J_1 = 1.1$ meV), and (i) a J_1–K model with $K = 0.18J_1$ ($J_1 = 1.1$ meV). (i) Momentum dependence of the low-energy inelastic signal $0.9 \leq E \leq 1.4$ meV (black dots) and comparison to linear spin-wave-theory predictions for optimized parameters from the J_1–J_1' XXZ (solid red line) and J_1–K models (dashed blue line). To avoid over subtraction, the cut is taken from empty cryostat subtracted data while (f) shows a temperature subtracted spectrum.

$\mathcal{H}_{ex} \equiv J\sum_{ij}(S_i^x S_j^x + S_i^y S_j^y + \Delta S_i^z S_j^z)$, opens a gap in the spectrum and yields an excellent agreement with the data for $J_1 = J_1' = 1.06$ meV and $\Delta = 1.22$ [Fig. 3(g)]. Allowing J_1' to vary independently slightly broadens the bandwidth but does not significantly improve the agreement between data and calculations [Fig. 3(h)]. Introducing a Kitaev term K in the Hamiltonian yields an overall agreement with the data for $J_1 = 1.1$ meV ($J_1' = J_1$) and an antiferromagnetic $K = 0.18J_1$, but introduces a weak double-gap feature at the band bottom that is clearly not observed in the experiment [Fig. 3(i)]. A cut through the low-energy part of the data and the corresponding spin-wave calculations [Fig. 3(j)] shows overall agreement, except between $Q = 0.25$ Å^{-1} and 1 Å^{-1} where background contributions are large. All models fail to account for the apparent continuum at the top of the band, which we attribute to the presence of quantum fluctuations. Although single-crystal studies will be necessary to determine the relative importance of these terms in detail.

In conclusion, the 1.1(1) meV energy scale of the Heisenberg exchange interaction in Na_2PrO_3 is surprisingly large for a lanthanide system, that is reflected in the large 230 meV scale of the crystal-electric field and the necessity to employ an intermediate-coupling scheme to explain the small effective moment of $1.0\mu_B$ per Pr^{4+}. In turn, these effects are hypothesized to be the origin of the considerably weaker antiferromagnetic Kitaev interaction, extracted by modeling the magnetic fluctuations of Na_2PrO_3, when compared to theoretical and *ab-initio* calculations [24]. The absence of visible magnetic Bragg peaks in Na_2PrO_3 as well as the missing entropy of around $0.3R\ln 2$ are two avenues for future inquiry. In particular, the observed low moment for the Pr^{4+} ion has important implications for the understanding and application of high-valence lanthanide ions in magnetic materials, since, akin to observations in high-valence actinides, this moment is derived from competition between SOC and CEF and necessitates the use of an intermediate coupling scheme to capture the observed temperature dependence [44, 45].

We thank Zhiling Dun for numerous helpful discussions. The work of A.R. and H.S.L. at Georgia Tech was supported by the Beckman Foundation as part of a Beckman Young Investigator Award to H.S.L. The work of M.D. and M.M. at Georgia Tech was supported by the National Science Foundation through grant NSF-DMR-

1750186. This research used resources at the High Flux Isotope Reactor and Spallation Neutron Source, a DOE Office of Science User Facility operated by the Oak Ridge National Laboratory.

* These two authors contributed equally
† mourigal@gatech.edu
‡ hsl@gatech.edu

[1] L. Balents, Nature **464**, 199 (2010).
[2] C. Broholm, R. Cava, S. Kivelson, D. Nocera, M. Norman, and T. Senthil, Science **367** (2020).
[3] R. Sibille, E. Lhotel, V. Pomjakushin, C. Baines, T. Fennell, and M. Kenzelmann, Phys. Rev. Lett. **115**, 097202 (2015).
[4] K. Kimura, S. Nakatsuji, J. Wen, C. Broholm, M. Stone, E. Nishibori, and H. Sawa, Nat. Commun. **4**, 1934 (2013).
[5] J. A. Paddison, M. Daum, Z. Dun, G. Ehlers, Y. Liu, M. B. Stone, H. Zhou, and M. Mourigal, Nat. Phys. **13**, 117 (2017).
[6] M. M. Bordelon, E. Kenney, C. Liu, T. Hogan, L. Posthuma, M. Kavand, Y. Lyu, M. Sherwin, N. P. Butch, C. Brown, M. J. Graf, L. Balents, and S. D. Wilson, Nat. Phys. **15**, 1058 (2019).
[7] Z. Dun, X. Bai, J. A. Paddison, E. Hollingworth, N. P. Butch, C. D. Cruz, M. B. Stone, T. Hong, F. Demmel, M. Mourigal, et al., Phys. Rev. X **10**, 031069 (2020).
[8] R. Sibille, N. Gauthier, E. Lhotel, V. Porée, V. Pomjakushin, R. A. Ewings, T. G. Perring, J. Ollivier, A. Wildes, C. Ritter, T. C. Hansen, D. A. Keen, G. J. Nilsen, L. Keller, S. Petit, and T. Fennell, Nat. Phys. **16**, 546 (2020).
[9] A. Kitaev, Ann. Phys. **321**, 2 (2006).
[10] J. Chaloupka, G. Jackeli, and G. Khaliullin, Phys. Rev. Lett **105**, 027204 (2010).
[11] Y. Singh, S. Manni, J. Reuther, T. Berlijn, R. Thomale, W. Ku, S. Trebst, and P. Gegenwart, Phys. Rev. Lett. **108**, 127203 (2012).
[12] Y. Motome, R. Sano, S. Jang, Y. Sugita, and Y. Kato, J. Phys.: Condens. Matter (2020).
[13] H. Takagi, T. Takayama, G. Jackeli, G. Khaliullin, and S. E. Nagler, Nat. Rev. Phys. (2019).
[14] A. Banerjee, C. Bridges, J.-Q. Yan, A. Aczel, L. Li, M. Stone, G. Granroth, M. Lumsden, Y. Yiu, and J. Knolle, Nat. Mater. **15**, 733 (2016).
[15] A. Banerjee, J. Yan, J. Knolle, C. A. Bridges, M. B. Stone, M. D. Lumsden, D. G. Mandrus, D. A. Tennant, R. Moessner, and S. E. Nagler, Science **356**, 1055 (2017).
[16] S. Choi, R. Coldea, A. Kolmogorov, T. Lancaster, I. Mazin, S. Blundell, P. Radaelli, Y. Singh, P. Gegenwart, and K. Choi, Phys. Rev. Lett **108**, 127204 (2012).
[17] K. Kitagawa, T. Takayama, Y. Matsumoto, A. Kato, R. Takano, Y. Kishimoto, S. Bette, R. Dinnebier, G. Jackeli, and H. Takagi, Nature **554**, 341 (2018).
[18] T. Takayama, A. Kato, R. Dinnebier, J. Nuss, H. Kono, L. Veiga, G. Fabbris, D. Haskel, and H. Takagi, Phys. Rev. Lett. **114**, 077202 (2015).
[19] R. Sano, Y. Kato, and Y. Motome, Phys. Rev. B **97**, 014408 (2018).
[20] H. Liu and G. Khaliullin, Phys. Rev. B **97**, 014407 (2018).
[21] F.-Y. Li, Y.-D. Li, Y. Yu, A. Paramekanti, and G. Chen, Phys. Rev. B **95**, 085132 (2017).
[22] J. G. Rau and M. J. Gingras, Phys. Rev. B **98**, 054408 (2018).
[23] G. Sala, M. Stone, B. K. Rai, A. May, P. Laurell, V. Garlea, N. Butch, M. Lumsden, G. Ehlers, and G. Pokharel, arXiv preprint arXiv:2003.01754 (2020).
[24] S.-H. Jang, R. Sano, Y. Kato, and Y. Motome, Phys. Rev. B **99**, 241106 (2019).
[25] T. P. Gompa, A. Ramanathan, N. T. Rice, and H. S. La Pierre, Dalton Trans., Advance Article, DOI: 10.1039/D0DT01400A (2020).
[26] S. G. Minasian, E. R. Batista, C. H. Booth, D. L. Clark, J. M. Keith, S. A. Kozimor, W. W. Lukens, R. L. Martin, D. K. Shuh, S. C. E. Stieber, T. Tylisczcak, and X.-d. Wen, J. Am. Chem. Soc. **139**, 18052 (2017).
[27] A. Ramanathan, J. E. Leisen, and H. S. La Pierre, Submitted.
[28] G. E. Granroth, A. I. Kolesnikov, T. E. Sherline, J. P. Clancy, K. A. Ross, J. P. C. Ruff, B. D. Gaulin, and S. E. Nagler, J. Phys.: Conf. Series **251**, 012058 (2010).
[29] M. B. Stone, J. L. Niedziela, D. L. Abernathy, L. DeBeer-Schmitt, G. Ehlers, O. Garlea, G. E. Granroth, M. Graves-Brook, A. I. Kolesnikov, A. Podlesnyak, and B. Winn, Rev. Sci. Instrum. **85**, 045113 (2014).
[30] O. Arnold, J. Bilheux, J. Borreguero, A. Buts, S. Campbell, L. Chapon, M. Doucet, N. Draper, R. F. Leal, M. Gigg, V. Lynch, A. Markvardsen, D. Mikkelson, R. Mikkelson, R. Miller, K. Palmen, P. Parker, G. Passos, T. Perring, P. Peterson, S. Ren, M. Reuter, A. Savici, J. Taylor, R. Taylor, R. Tolchenov, W. Zhou, and J. Zikovsky, Nucl. Instrum. Methods Phys. Res., Sect. A **764**, 156 (2014).
[31] S. Kern, C.-K. Loong, and G. H. Lander, Phys. Rev. B **32**, 3051 (1985).
[32] V. Kaufman and J. Sugar, J. Res. Natl. Bur. Stand. A Phys. Chem. **71**, 583 (1967).
[33] Y. Hinatsu and N. Edelstein, J. Solid State Chem. **112**, 53 (1994).
[34] A. Boothroyd, "Spectre, a program for calculating spectroscopic properties of rare earth ions in crystals(1990–2014),".
[35] J. Chaloupka, G. Jackeli, and G. Khaliullin, Phys. Rev. Lett **110**, 097204 (2013).
[36] M. Bickel, G. Goodman, L. Soderholm, and B. Kanellakopulos, J. Solid State Chem. **76**, 178 (1988).
[37] Y. Hinatsu and Y. Doi, J. Alloys Compd. **418**, 155 (2006).
[38] V. O. Garlea, B. C. Chakoumakos, S. A. Moore, G. B. Taylor, T. Chae, R. G. Maples, R. A. Riedel, G. W. Lynn, and D. L. Selby, Appl. Phys. A **99**, 531 (2010).
[39] K. Kimura, S. Nakatsuji, J. Wen, C. Broholm, M. Stone, E. Nishibori, and H. Sawa, Nat. commun. **4**, 1 (2013).
[40] A. S. Wills, Phys. B (Amsterdam, Neth.) **276–278**, 680 (2000).
[41] J. Rodríguez-Carvajal, Phys. B (Amsterdam, Neth.) **192**, 55 (1993).
[42] S. Petit, Collection SFN **12**, 105 (2011).
[43] S. Toth and B. Lake, J. Phys.: Condens. Matter **27**, 166002 (2015).
[44] N. Magnani, P. Santini, G. Amoretti, and R. Caciuffo, Phys. Rev. B **71**, 054405 (2005).
[45] L. Escalera-Moreno, J. J. Baldoví, A. Gaita-Ariño, and E. Coronado, Inorg. Chem. **58**, 11883 (2019).

Collective excitations in the tetravalent lanthanide honeycomb antiferromagnet, Na_2PrO_3

M. J. Daum,[1] A. Ramanathan,[2] A. I. Kolesnikov,[3] S. Calder,[3] M. Mourigal,[1] and H. S. La Pierre[2,4]

[1] School of Physics, Georgia Institute of Technology, Atlanta, GA 30332, USA

[2] School of Chemistry and Biochemistry, Georgia Institute of Technology, Atlanta, GA 30332, USA

[3] Neutron Scattering Division, Oak Ridge National Laboratory, Oak Ridge, TN 37831, USA

[4] Nuclear and Radiological Engineering and Medical Physics Program, School of Mechanical Engineering, Georgia Institute of Technology, Atlanta, GA 30332, USA

1. Sample preparation and structural characterization.

Polycrystalline samples of Na_2LnO_3 were synthesized and structurally characterized as reported in Ref 1.[1] The structure of Na_2LnO_3 solved using the *C*2/*c* space group. The synchrotron powder X-ray diffraction patterns indicate 6L peaks evident of *C*2/*c* stacking. Due to the reduced intensity of 6L peaks, however, it is possible model the system using an incoherent distribution of domains of both *C*2/*m* and *C*2/*c* stacking either due to twinning or intergrowth since a stacking fault at the boundary of two *C*2/*c* domains could result in a *C*2/*m* domain. However, to include the stacking faults and all types of stacking sequences in the material, the larger unit cell of *C*2/*c* has been chosen in the following analysis.

Synthesis of Na_2LnO_3 (Ln = Ce, Pr, Tb). A typical reaction yields ~ 0.8 g of samples. Therefore, for each Na_2LnO_3 sample, 10 reactions were carried out and the resulting powder samples were mixed yielding ~ 8 g of Na_2PrO_3, Na_2CeO_3, and Na_2TbO_3.

2. High-energy INS with flat bands of OH stretches.

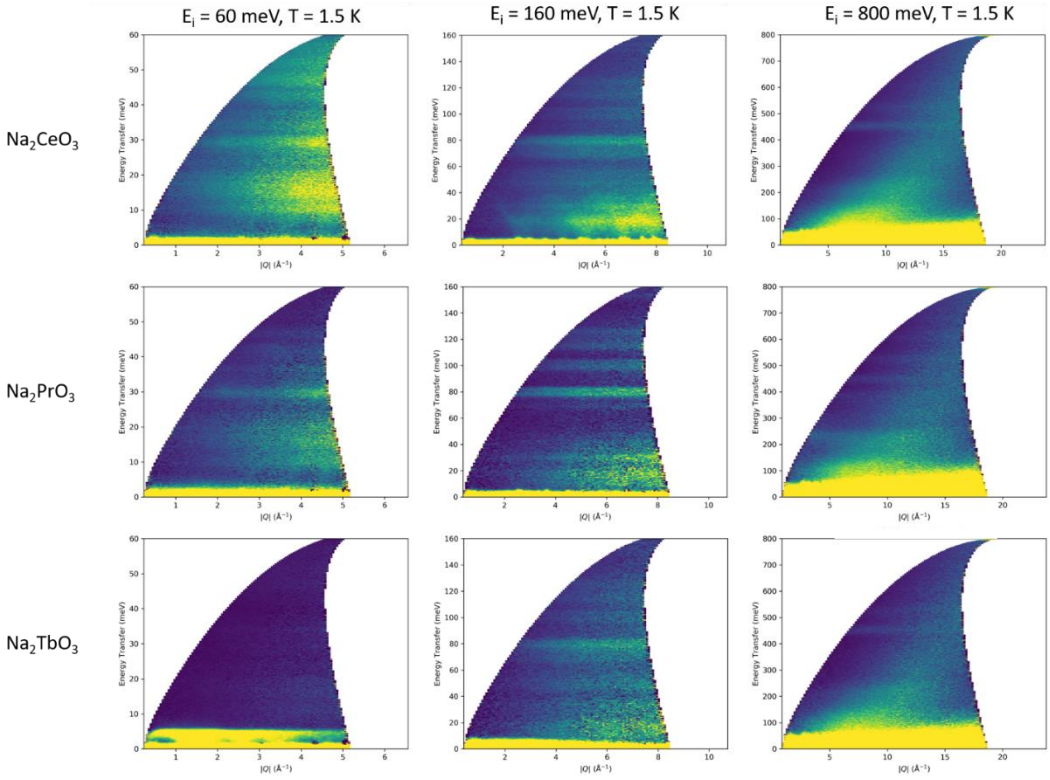

Figure S1. Overview of inelastic neutron scattering data measured on SEQUOIA for Na_2CeO_3 (first row), Na_2PrO_3 (second row), Na_2TbO_3 (third row) with incident energies E_i = 60 meV (first column), 160 meV (second column) and 800 meV (third column). The 800 meV data shows a hydrogen recoil line as well as OH stretching modes that we traced back to a minute amount of NaOH in the starting materials.

Broadband inelastic neutron scattering measurements using E_i = 60, 160, and 800 meV revealed a number of flat modes, common across all three compounds, Na_2LnO_3 (Ln = Ce, Pr, Tb), see Figure S1. The flat modes are attributed to vibrational excitations and the dispersive background visible in the E_i = 800meV is attributed to a hydrogen recoil line with the clear quadratic, Q^2, dependence typical of recoil processes and previously observed by Sensei *et al*[2, 3]. At energies above around 400 meV, the flat modes are in the frequency range of OH stretching mode from a NaOH impurity in the starting materials and identified to be < 3 wt% from laboratory powder X-ray diffraction of the Na_2O starting material. The OH stretches show a strong *Q* dependence at higher *Q* ruling them out as CEF transitions. After accounting for the OH stretching mode, we were able to identify one clear crystal-electric field transition (discussed in Section 3).

3. Crystal-electric field measurements.

Inelastic neutron scattering measurements were carried out on ~8 g of polycrystalline samples of Na_2LnO_3 (Ln = Ce, Pr, and Tb) on the time-of-flight fine-resolution Fermi chopper spectrometer SEQUOIA, at the Spallation Neutron Source, ORNL[4]. The powder samples were enclosed in a standard 15-mm diameter cylindrical aluminum cans under one atmosphere of ^{4}He at room temperature. All three samples were cooled using a closed-cycle refrigerator reaching a base temperature of T = 1.8 K. Measurements were carried out using incident neutron energies E_i = 300, 500, 800 at T = 15 K. Background and sample holder contributions were measured using empty can measurements. The lattice phonon contributions for Na_2PrO_3 and Na_2TbO_3 were subtracted by measuring the diamagnetic analog Na_2CeO_3.

The crystal field splitting of Pr^{4+} in Na_2PrO_3 was evaluated by comparing the INS spectrum to the isostructural Na_2TbO_3 and Na_2CeO_3 spectrum. After accounting for OH signals from the minor NaOH impurity (see SI Section 2), only one CEF level for Pr^{4+} centered ~230 meV and no CEF level for Tb^{4+} are observed.

CEF splitting scheme for Pr^{4+}:

The strong spin orbit coupling of Pr^{4+}, a $4f^1$ ion, entangles the electron spin, S = ½ and high orbital angular momentum L = 3 to give rise to a J = 5/2 ground state ($^2F_{5/2}$) and a J = 7/2 excited state ($^2F_{7/2}$)[5, 6]. The six-fold degeneracy of the $^2F_{5/2}$ ground state is removed under the crystal-electric field. Under a highly symmetric O_h point group symmetry, the $^2F_{5/2}$ ground state is split into a doublet Γ_7 and a quartet Γ_8. However, any deviation from the O_h symmetry will remove the degeneracy of the Γ_8 state resulting a maximum splitting of $^2F_{5/2}$ state into three Kramers doublets[5]. The observation of one CEF level in the INS spectrum might indicate a doublet ground state with a quartet excited state. However, the site symmetry of the Pr^{4+} in Na_2PrO_3 is D_{2d} (rather than O_h). This lower point symmetry splits the $^2F_{5/2}$ ground state into three Kramers doublets, thus yields two excited doublets with an energy separation proportional to the distortion from ideal O_h point symmetry. Therefore, the observed CEF level in the INS spectrum likely encompasses two Kramers doublets that are not resolved within the resolution of the instrument. This model is further supported from CEF calculations (*vide infra*). INS data at low energies shows no further features which rules out the possibility of a low-lying CEF level and placing the ~230 meV CEF level as the first CEF transition. A similar observation has been made for Pr^{4+} in $BaPrO_3$ using INS data[7]. INS experiment with an incoming energy E_i = 800 meV did not reveal any higher energy CEF levels but the restricted kinematic range of our measurements above 500 meV as well as the elevated background above 400 meV due to OH stretching modes does not allow us to conclude on the existence of visible CEF excitations above 500 meV.

Table S1. Calculated CEF eigen-energies and the corresponding wavefunction using the *LS*-coupling scheme. The best CEF Wybourne parameters used for the calculations are B_0^2 = 300 meV, B_0^4 = 120 meV.

***E* (meV)**	$\|^2F_{5/2}, m_j\rangle$					
	+1/2	**-1/2**	**+3/2**	**-3/2**	**+5/2**	**-5/2**
0	0	0	-0.515	-0.173	0.250	0.742
228.3	0	0	-0.383	0.618	0.428	-0.266
234.1	-0.440	0.783	0	0	0	0

Table S2. Calculated CEF eigen-energies and the corresponding wavefunction using the intermediate coupling scheme. The best CEF Wybourne parameters used for the calculations are B_0^2 = 175 meV, B_0^4 = 180 meV, B_0^6 = -9 meV.

***E* (meV)**		**0**	**237**	**242.8**	**532.3**	**540.3**	**721.3**	**792.1**
$\|^2F_{5/2}, m_j\rangle$	**+1/2**	0	0.701	0	0	-0.349	-0.086	0
	-1/2	0	-0.431	0	0	0.054	-0.041	0
	+3/2	0.630	0	0.350	-.346	0	0	-0.135
	-3/2	0.265	0	-0.139	-0.388	0	0	-0.078
	+5/2	-0.225	0	-0.243	-0.253	0	0	0.008
	-5/2	-0.535	0	0.615	0.160	0	0	0.014
$\|^2F_{7/2}, m_j\rangle$	**+1/2**	0	-/088	0	0	-0.532	0.690	0
	-1/2	0	-0/054	0	0	0.082	-0.326	0
	+3/2	-0.056	0	-0.322	0.287	0	0	0.543
	-3/2	0.023	0	-0.128	0.453	0	0	-0.311
	+5/2	-0.096	0	0.157	-0.366	0	0	-0.308
	-5/2	0.229	0	0.397	-0.232	0	0	0.538
	+7/2	0	0.163	0	0	0.742	-0.215	0
	-7/2	0	0.266	0	0	-0.114	0.455	0

Since only one CEF transition was observed, no attempt was carried out to fit the neutron data for extracting the CEF parameters (since the CEF parameters can be determined by inspecting the relative intensities of transitions in INS data). However, the CEF parameters were extracted by calculating magnetic susceptibility using the SPECTRE program by placing careful constraints from the INS data[8].

In a O_h crystal field, the Hamiltonian for the CEF (H_{CEF}) is given by

$$H_{CEF} = B_0^4 C_0^4 + B_4^4 C_4^4 + B_0^6 C_0^6 + B_4^6 C_4^6 \quad (1)$$

where B_q^k (k, q are integers and k≥q) are crystal field parameters and C_q^k are components of Wybourne tensor operator[9]. Given the high symmetry, the Hamiltonian can be further simplified by taking B_4^4 = $0.5976B_0^4$ and B_4^6 = $-1.871B_0^6$ resulting in equation (2) with two independent parameters.

$$H_{CEF} = B_0^4 (C_0^4 + 0.5976C_4^4) + B_0^6 (C_0^6 - 1.871C_4^6) \quad (2)$$

Since the true point symmetry of Pr^{4+} could be best described using D_{2d}, an axial term $B_0^2 C_0^2$ was added to the Hamiltonian to account for the reduction in symmetry from O_h. Constraints on B_4^4 and B_4^6 as in Equation 2 were retained to retain the proximate O_h crystal field with the axial distortion as a perturbation. The effective CEF Hamiltonian is thus written with three independent parameters as

$$H_{CEF} = B_0^2 C_0^2 + B_0^4 (C_0^4 + 0.5976C_4^4) + B_0^6 (C_0^6 - 1.871C_4^6) \quad (3)$$

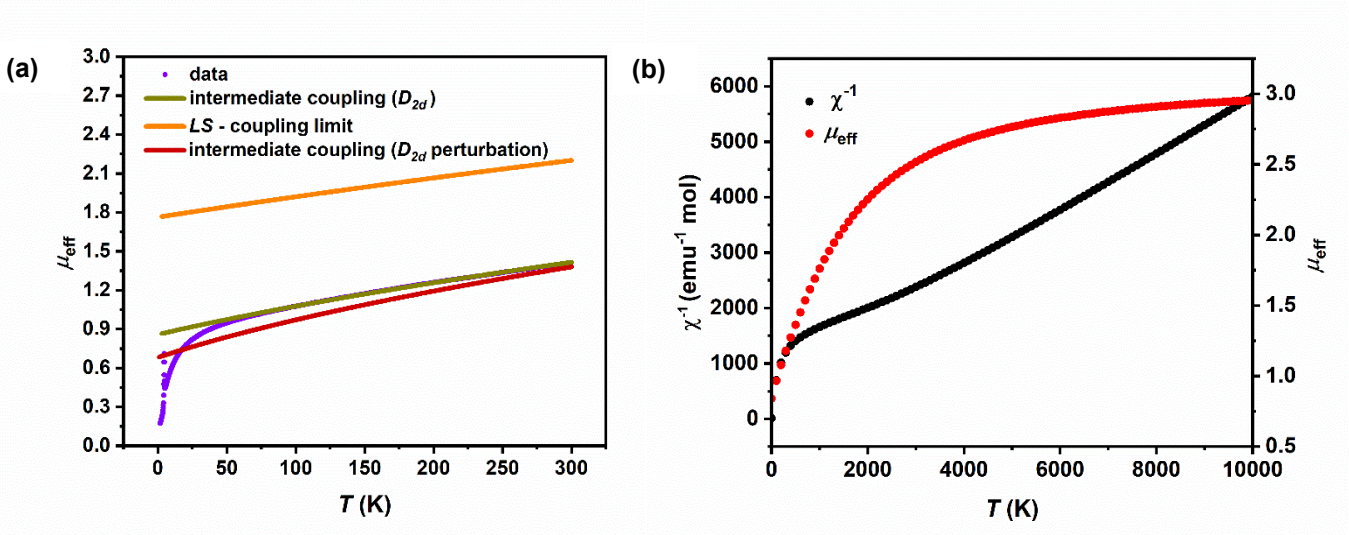

Figure S2. (a) Experimental and calculated magnetic moment as a function of temperature. The experimental effective magnetic moments were calculated from bulk susceptibility measurements. (b) Calculated inverse susceptibility and magnetic moment up to 10000 K.

Since Pr exhibits an unusual valence state of 4+, a CEF model was developed analogous to isoelectronic Ce^{3+}. For Ce^{3+} all sixth order B_0^6 and B_4^6 terms are zero resulting in two independent parameters (B_0^2 and B_0^4) in the *LS* coupling limit. Since fitting of the neutron data was not pursued to extract the CEF parameters, magnetic susceptibility for different values of the CEF parameters was calculated using SPECTRE and compared to experimental data.[8] With this scheme, magnetic susceptibility was calculated for different values of B_0^2 and B_0^4 in Hamiltonian 3 by constraining the first excited state CEF level to be ~ 230 meV (as observed from INS data). However, the magnetic susceptibility calculated in the *LS* coupling limit does not provide a good match with the experimental susceptibility data (Figure S2). The closest set of CEF parameters to provide a reasonable match produces the ground state doublet wavefunction shown in Table S1. In the Ce^{3+} model, Pr^{4+} was treated as a traditional trivalent lanthanide with SOC being the dominant interaction. However, since the observed first excited state at 230 meV is on the same energy scale as the SOC separation between $^2F_{5/2}$ and $^2F_{7/2}$ manifolds for Pr^{4+},[10, 11] a second CEF model (D_{2d} perturbation model) was developed by including the complete set of 14 intermediate-coupling basis sets, required given the comparable strengths of CEF and SOC interactions in lanthanides (Equation 3).

The intermediate coupling calculations were carried out by taking in to account the excited state multiplet $^2F_{7/2}$ which is expected to split into four Kramers doublets. With this scheme, B_0^6 and B_4^6 terms are constrained by symmetry since we introduce the axial distortion as a perturbation on the O_h crystal field. The magnetic susceptibility was calculated for different values of B_0^2 , B_0^4, and B_0^6 in Hamiltonian 3 by constraining the first excited state CEF level to be ~ 230 meV. The calculated susceptibility provides a better approximation of the experimental data compared to the Ce^{3+} CEF model indicating the importance of intermediate coupling (Figure S2). However, there is notable deviation between the calculated and experimental susceptibility and can be attributed to the symmetry constraints in Equation 3. Equation 3 was derived based on the approximation that the axial distortion acts as a perturbation on O_h crystal field resulting in B_4^4 = 0.5976 B_0^4 and B_4^6 = -1.871 B_0^6 constraints. A third CEF model (D_{2d} model) was created by removing the symmetry constraints in Equation 3. The corresponding CEF Hamiltonian is defined by five independent parameters as

$$H_{CEF} = B_0^2 C_0^2 + B_0^4 C_0^4 + B_4^4 C_4^4 + B_0^6 C_0^6 + B_0^6 C_4^6 \quad (4)$$

From this third CEF model, the calculated magnetic susceptibility provides a better match to the experimental data compared to the other models. The ability of this CEF scheme to model the experimental susceptibility can be attributed to treating the symetry at Pr^{4+} as D_{2d} rather than a perturbation on O_h.This essentially calls for the importance of distortion to the PrO_6 octahedron as a key ingredient in determining

the single-ion and bulk behavior in Pr^{4+} materials. From this CEF scheme (D_{2d} model), the obtained ground-state is a doublet dominated by $|^2F_{5/2} \pm 3/2\rangle$ and $|^2F_{7/2} \pm 5/2\rangle$ states. A similar wavefunction with different mixing coefficients was obtained for D_{2d} perturbation CEF scheme. However, in the *LS* coupling limit, only mixing with in the J=5/2 manifold was observed. This clearly indicates mixing between different CEF states is essential to describe the single-ion behavior of Pr^{4+} ions and is attributed to the comparable energy scale of CEF to SOC. The complete list of CEF parameters and wavefunctions are provided in Table S2. It should be noted here that the D_{2d} model suffers from over parametrization since only one CEF level was observed from INS. This essentially provides three constraints (the quasi-degenerate CEF level and magnetic susceptibility) with five independent variables. The exact mixing coefficients can be calculated only if all CEF are observed which is difficult with INS because of high energy CEF excitations.

The calculated magnetic susceptibility (from all three models) as a function of temperature is plotted in Figure S2a and compared against the experimental data. It should be noted here that the magnetic susceptibility is provided as effective magnetic moment $\mu_{eff} = \left(\left(\frac{3k_B}{N_A\mu_B^2}\right) * \chi T\right)^{1/2} \sim 2.828\ \sqrt{\chi T}$ for better discrimination between the models. As expected, the room-temperature moment for the Ce^{3+} CEF model is close to the free ion moment of 2.54 μ_B. However, it does not provide a good match with the experimental data. The intermediate coupling model with 5 parameters provides a reasonable agreement with the experimental data for T≥ 60 K, below which the system deviates from the single-ion limit. The intermediate coupling model also accounts for the small magnetic moment of Pr^{4+}.

The inability to identify a linear region in $1/\chi$ data for Na_2PrO_3 (discussed in the main text; Figure 1(d)) is attributed to the effect of CEF. Even though the first excited state is at 230 meV, the CEF has significant contribution to magnetic susceptibility down to ~100 K. Therefore, we calculated magnetic susceptibility as a function of temperature up to 10000 K (Figure S2). It is evident that ~ 2800 K, the magnetic moment reached ~2.5 μ_B close to the expected value for a f^1 ion. A linear region in $1/\chi$ data is obtained only after ~ 3000 K.

4. ac Susceptibility.

To rule out the possibility of a spin freezing, alternating current (ac) magnetic susceptibility measurements were carried out. Figure S3 shows the ac magnetic susceptibility data as function of temperature at different frequencies. There is no noticeable frequency-dependence in the in-phase susceptibility, χ', and the out of phase component, χ'', remains zero at all temperatures. This measurement rules out the possibility of a spin glass in Na_2PrO_3.

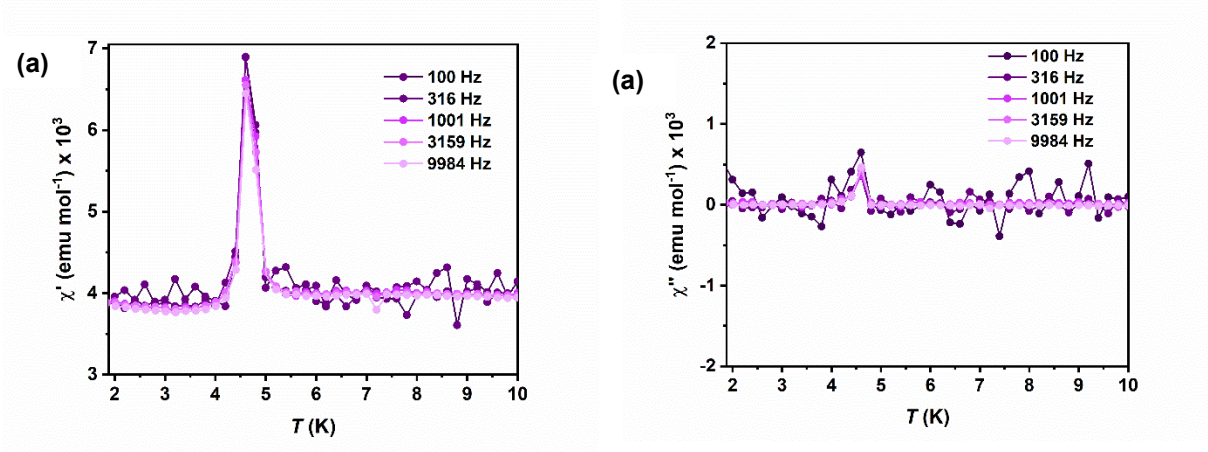

Figure S3. ac Magnetic susceptibility of Na_2PrO_3 showing the real part (a), and imaginary part (b) as a function of temperature with no observable frequency dependence.

5. Specific heat analysis.

The heat capacity of Na_2PrO_3 was measured in zero magnetic field using a Quantum Design Physical Properties Measurement System and is shown in Figure 2a. For T > 2 K the data were acquired using the standard PPMS cryogenic platform. For 0.09 K < T < 4 K a Quantum Design dilution fridge insert was employed.

The total specific heat C_P, in insulating Na_2PrO_3 encompasses: C_L, the lattice specific heat, C_M, the magnetic specific heat and, C_N, the nuclear contribution. C_L was approximated by C_P measured for the non-magnetic analog Na_2CeO_3 (shown in Figure 2a) after correction for the different unit cell masses.

The total specific heat C_P for Na_2PrO_3 clearly shows a λ like anomaly at 4.6 K associated with long range magnetic order. However, below 0.9 K, there is an upturn which can be associated with nuclear spin degrees of freedom. The nuclear contribution encompasses both dipole and quadrupole hyperfine splitting contributions for a ^{141}Pr nucleus which carries a nuclear spin quantum number I = 5/2. The quadrupolar term is neglected given that the quadrupole moment of the ^{141}Pr nucleus is small (0.0589 barn) with negligible contribution for T < 0.9 K[12, 13]. The nuclear contribution to the specific heat is modeled (equation S4) assuming a dipolar hyperfine splitting of the nuclear spin states. Give that our CEF analysis yields electronic moments with predominantly Ising anisotropy at low temperatures, the following Schottky anomaly was used model the nuclear contribution to specific heat:

$$C_{sch} = Nk_B \frac{\alpha^2}{4I^2}\left[\frac{1}{sinh^2(\alpha/2I)} - \frac{(2I+1)^2}{sinh^2\left((2I+1)\alpha/2I\right)}\right] \quad (4)$$

$$\alpha = A_{hf}\left(\mu_{hyp}^{(\mathrm{Pr})}/g_J\right) I/k_B T \quad (5)$$

where, N and k_B are Avogadro's number and the Boltzmann constant, I = 5/2 and A_{hf} = 0.078 T are the nuclear spin and hyperfine coupling constant for ^{141}Pr nucleus. g_J = 6/7 and $\mu_{hyp}^{(\mathrm{Pr})}$ are Lande's g factor and the static Pr^{4+} magnetic dipole moment at the T_1 relaxation time scale. Equation S4 provides excellent fit to the T < 0.9 K data for $\mu_{hyp}^{(\mathrm{Pr})}$ = 0.41 μ_B as shown in Figure 2a.

The entropy recovered across the ordering transition was calculated by integrating only the magnetic specific heat for T > 0.9 K resulting in ΔS = ~0.71 Rln2. Even though the upturn below 0.9 K has been associated with nuclear contribution to specific heat, we cannot rule out contributions from the electronic spin degrees of freedom. Therefore, we calculated the entropy recovered by including the upturn below 0.9 K yielding ΔS = ~0.76 Rln2.

6. Magnetic structure refinement for Na_2TbO_3

The magnetic structure of Na_2TbO_3 was determined from the inelastic neutron scattering data. For reference, the susceptibility data of Na_2TbO_3 is shown in Figure S4 with a clear magnetic ordering transition around T_N = 37.7 K. By inspecting the elastic line of the E_i = 60 meV data at T = 19 and 55 K, we were able to extract two diffraction like patterns above and below the ordering temperature. Above the ordering temperature only the nuclear Bragg peaks contribute to intensity while below the ordering temperature there is contribution from both nuclear and magnetic Bragg peaks. The T = 55 K data was subtracted from 19 K data to reveal intense magnetic Bragg peaks. The pattern was then refined in FULLPROF assuming only a magnetic phase and indexed with the $\boldsymbol{k}_m$ = 0 propagation vector[14].

In Na_2TbO_3 there are two crystallographic unique Tb^{4+} sites, each lying on *4f* position in *C*2/*c* symmetry resulting in two equivalent positions per Tb site (a total of 4 sites) constrained by translation vector

Atom 1 : x, y, z
Atom 2 : x, -y, ½+z

Representation analysis using SARAh with $\boldsymbol{k}_m$ = 0 propagation vector yields four irreducible representations (IRs) with a total of 12 basis vectors (six per Tb site) as listed in Table S3[15].

Table S3. Symmetry allowed IRs for Tb^{4+} in Na_2TbO_3 for *C*2/*c* space group with $\boldsymbol{k}_m$ = 0 propagation vector.

IR	BV	Tb1						Tb2					
		Atom 1			Atom 2			Atom 1			Atom 2		
		m_x	m_y	m_z	m_x	m_y	m_z	m_x	m_y	m_z	m_x	m_y	m_z
1	Ψ_1	0	2	0	0	2	0	0	2	0	0	2	0
2	Ψ_1	0	2	0	0	-2	0	0	2	0	0	-2	0
3	Ψ_1	2	0	0	2	0	0	2	0	0	2	0	0
	Ψ_2	0	0	2	0	0	2	0	0	2	0	0	2
4	Ψ_1	2	0	0	-2	0	0	2	0	0	-2	0	0
	Ψ_2	0	0	2	0	0	-2	0	0	2	0	0	-2

IRs 1 and 3 correspond to ferromagnetic arrangement of the spins in the honeycomb-lattice place and can be ruled out since they result in peaks at low 2θ evidently not present in our data. Refinement with IR 2 did not result in a good fit. A reasonable fit to experimental data was obtained with IR 4 as shown in Figure 3e. Therefore, the magnetic structure was best described using IR 4 with the spins antiferromagnetically arranged in the honeycomb-lattice plane with a spin direction in the *ac*-plane and mostly aligned along the crystallographic *c*-direction as shown in Figure 1a. All refinements were carried out in range $3 < 2\theta < 27°$. A custom background was generated using the insert point background function in FULLPROF[14].

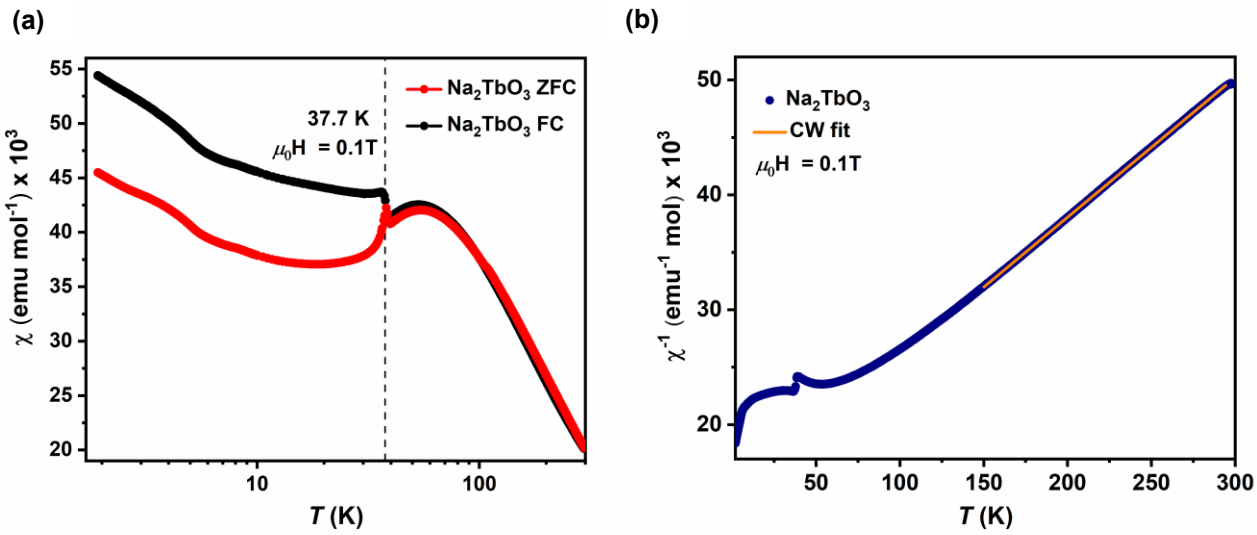

Figure S4. (a) ZFC and FC Magnetic susceptibility of Na_2TbO_3 showing a magnetic transition at T_N = 37.7 K, with a clear divergence between ZFC and FC below the transition temperature. (b) Inverse susceptibility (blue trace) of Na_2TbO_3 as a function of temperature with the Curie-Weiss fit (orange) yielding θ_{CW} = -112.7(1) K consistent with inelastic scattering measurement and μ_{eff} = 8.08 (2) μ_B in good agreement with the free-ion value.

7. Na_2TbO_3 Spin wave analysis.

The magnetic excitations of Na_2TbO_3, were modeled using the implementation of spin-wave theory in the Matlab program SpinW. In order to capture the apparent dispersion at the top of band, the minimal Hamiltonian includes split nearest-neighbor exchanges interactions J_1 and J_1',

$$\hat{H} = J_1 \sum_{i,j} \boldsymbol{S}_i \boldsymbol{S}_j + J_1' \sum_{i,j'} \boldsymbol{S}_i \boldsymbol{S}_{j'}$$

where $|J_1'|<|J_1|$ reflects the longer Tb-Tb distance on *d'* bonds (see Figure 1(a)). The determination of J_1 and J_1' proceeds by simulating a number of powder-averaged spectrum for values of J_1 and J_1' on a two-dimensional grid, and subsequently calculating the goodness of fit function χ^2 between the E_i = 8 meV data and the simulations convoluted with a constant energy resolution of 0.2 meV. The resulting χ^2 is shown in Fig. S7(a-b) where the best fit parameters J_1' = 0.50 meV and J_1' = 0.85 J_1 yield the spin-wave spectrum shown in Figure S5(c).

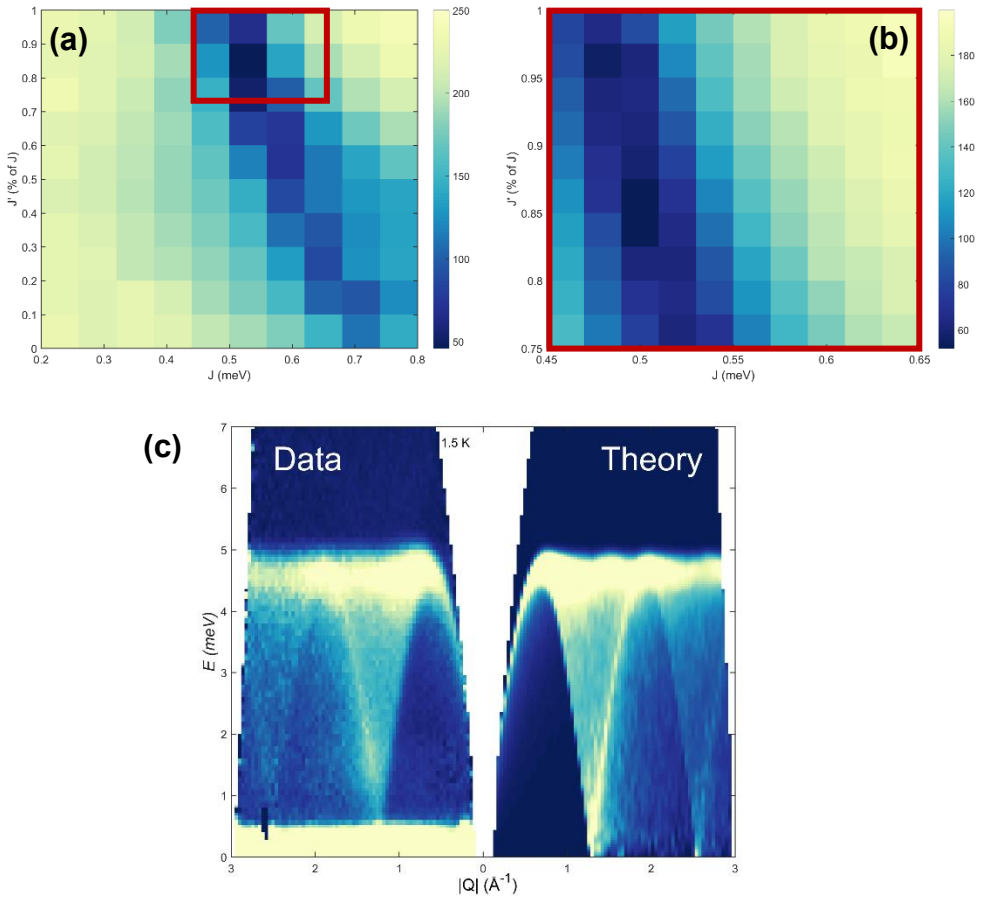

Figure S5. (a) Colormap of χ^2 results for different powder-averaged spin-wave calculations using an antiferromagnetic nearest neighbor J_1 and J_1' where J_1 varies from 0.2 meV to 0.8 meV and J_1' from 0 to 100% of J_1. The region of best fit is highlighted by a red square (b) Colormap of χ^2 focusing on the region of best fit from (a). **(c)** The "best fit" powder-averaged calculation for the J_1- J_1' model compared to experimental results on Na_2TbO_3.

The above Hamiltonian does not reproduce some of the details of the low-energy spectrum in Na_2TbO_3, in particular the precise magnetic structure observed experimentally and the concentration of neutron scattering intensity around 1 meV. Reproducing these features requires the addition of a small single-ion anisotropy term D, and an out-of-plane exchange interaction $J_\perp$ to the Hamiltonian,

$$\hat{H} = J_1 \sum_{i,j} \boldsymbol{S}_i \boldsymbol{S}_j + J_1' \sum_{i,j'} \boldsymbol{S}_i \boldsymbol{S}_{j'} + J_\perp \sum_{i,i'} \boldsymbol{S}_i \boldsymbol{S}_{i'} + D S_z^2$$

where $J_\perp$ connects Tb atoms on the same sublattice (*i.e.* $J_\perp$ links a Tb1 atom in one layer to a Tb1 atom in the next layer, and a Tb2 atom in one layer to a Tb2 atom in the next layer). The parameters are optimized by fixing the optimal value J_1' = 0.85 J_1 obtained in the previous fit, and letting J_1, D and $J_\perp$ vary on a three-dimensional grid, see Fig. S8. Ultimately, the minimal χ^2 value is found in the plane with J_1 = 0.50 meV for D = -0.001 J_1 and $J_\perp$ = -0.02 J_1 indicating uniaxial anisotropy and ferromagnetic coupling between planes, respectively. The resulting powder-averaged simulation for parameters corresponding to the minimal χ^2 is shown in Fig. 3 **c** of the main text. Although dipolar interactions are expected given the large magnetic dipole moment of the Tb^{4+} atoms, their effect is probably reflected in the small uniaxial anisotropy observed here.

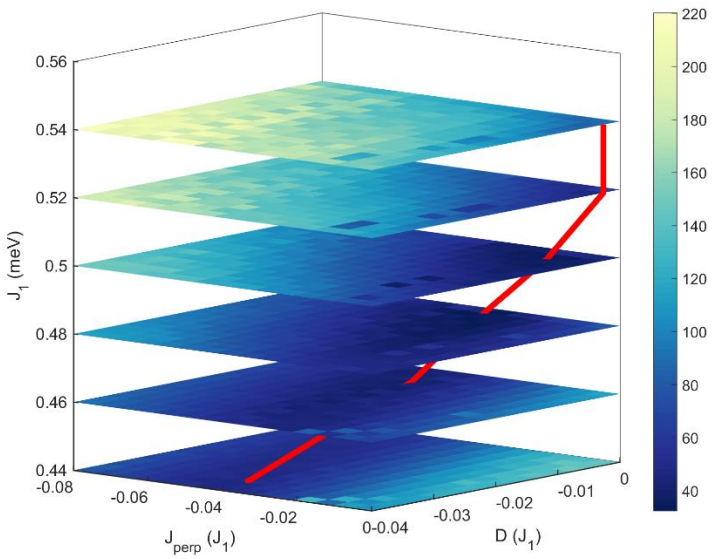

Figure S6. Colormap of χ^2 for the J_1- J_1'-D-$J_\perp$ model with varying D, $J_\perp$, and J_1 terms as seen on the x, y, and z-axes respectively. The red line denotes the minimal χ^2 value for each value of J_1.

The temperature dependence of the spin-wave excitations in Na_2TbO_3 across the ordering transition at T_N = 38.2 K is shown in Figure S7, revealing a transition to a broad paramagnetic response above T_N.

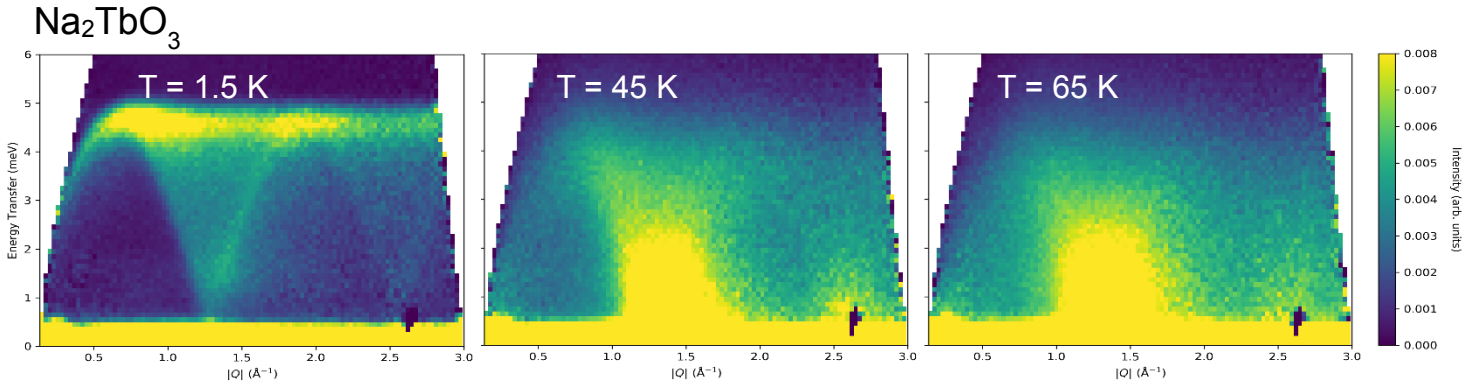

Figure S7. Temperature dependence of Na_2TbO_3 excitation at E_i = 20 meV.

8. Na_2PrO_3 Spin wave analysis.

A similar fitting strategy was used to model the magnetic excitations in Na_2PrO_3. Given the S_{eff}=1/2 nature of the magnetic moments, only exchange anisotropies are considered in this analysis. Given the large gap of ~1 meV in the excitation spectrum when compared to the total band-top energy of ~2 meV, the analysis starts with a simple J_1-J_1' model with an easy-axis XXZ exchange anisotropy, adopted to gap the excitation spectrum and consistent with the $g_{zz}>g_{xz}$ g-tensor extracted from our crystal-field analysis. The Hamiltonian reads:

$$\hat{H} = J_1 \sum_{i,j} S_i^x S_j^x + S_i^y S_j^y + (1+Z) S_i^z S_j^z + J_1' \sum_{i,j'} S_i^x S_{j'}^x + S_i^y S_{j'}^y + (1+Z) S_i^z S_{j'}^z$$

where Z>0 is the degree of easy-axis anisotropy. Calculations of the powder-averaged spectrum were performed as a function of parameters J_1, J_1', and Z on a three-dimensional grid. The goodness of fit function χ^2 between the E_i = 8 meV data (subtracted for the sample background at T=55 K) and the simulations was subsequently calculated and shown in Figure S8.

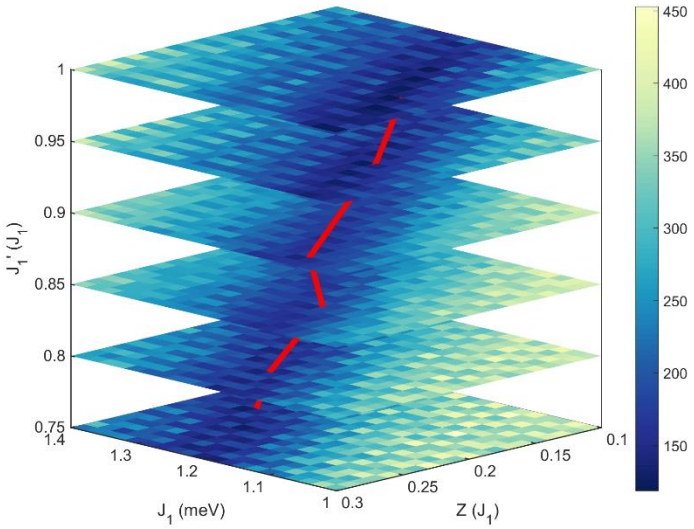

Figure S8. Colormap of χ^2 for the J_1-J_1' XXZ model with varying J_1, J_1' and Z parameters seen on the x, y, and z-axes, respectively. The red line denotes the minimal χ^2 value for each value of J_1'.

The absolute χ^2 minimum of Figure S8 is obtained for J_1' = J_1 what corresponds to the results shown in Figure 3(g) of the main manuscript. The presence of a possible weak continuum of excitation above the band top in Na_2PrO_3 leads to a slight overshoot of the excitation bandwidth shown in Figure S9. For this reason, a model with J_1' = 0.85 J_1 leads to a slightly better result by eye, as shown in Figure S9 and Figs. 3(g) and 3(h). Without further single-crystal experiments, it is difficult to know if separating the values of J_1 and J_1' is needed to explain the excitations of Na_2PrO_3.

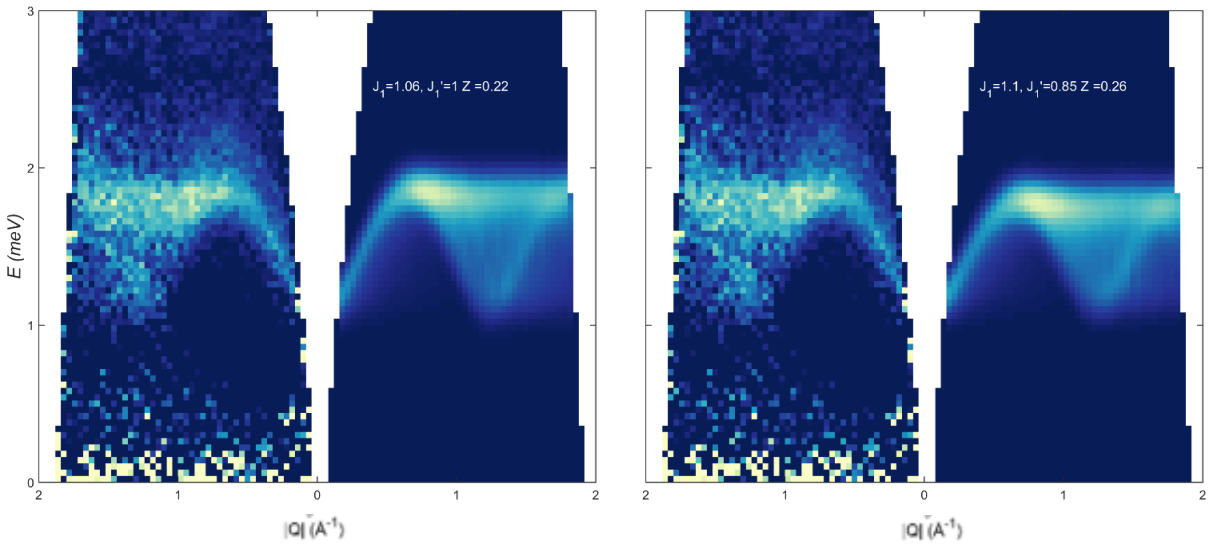

Figure S9. Closer inspection comparing J_1 XXZ (left) and J_1 - J_1' XXZ (right) models with the temperature subtracted data at E_i = 8 meV.

The final model introduced in the manuscript is the $J_1 - J_1' - K$ model representing the following Hamiltonian:

$$\hat{H} = J_1 \sum_{i,j} \boldsymbol{S}_i \boldsymbol{S}_j + J_1' \sum_{i,j'} \boldsymbol{S}_i \boldsymbol{S}_{j'} + K \sum_{i,j} S_i^{\gamma} S_j^{\gamma}$$

where K is the bond dependent Kitaev interaction, which is assumed to scale with the corresponds diagonal exchange (J_1 or J_1'). Starting with the ratio J_1'/J_1 = 0.85 of Na_2TbO_3, powder-averaged calculations were performed on a $J_1 - J_1' - K$ grid in order to find a general range of potential K values. Using this preliminary optimization for K, a χ^2 grid search was performed as a function of J_1 and J_1' resulting in an optimal value of $J_1' = 0.75\ J_1$. Using this ratio, a subsequent χ^2 grid search shown in Figure S10(a) as a function of J_1 and K yielded the best parameters J_1 = 1.4 meV and $K = 0.02\ J_1$. One feature of this model which is not seen in the experimental data is the secondary intensity seen in Figure S10(b) below 0.8 meV and corresponding to the presence of two distinct energy gaps in the spectrum. Although this feature may exist below the noise level of our experiment, the current data does not support its existence.

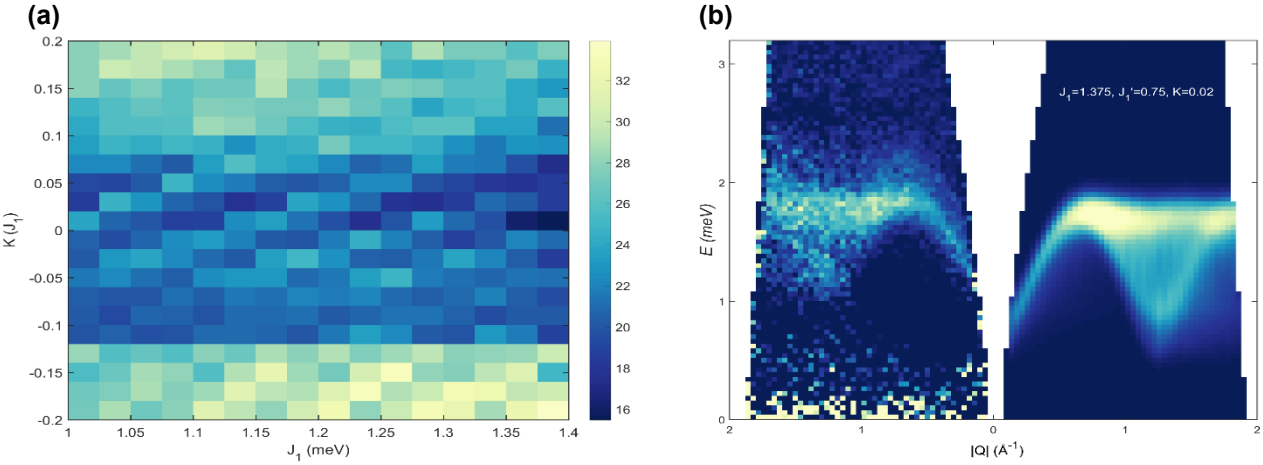

Figure S10. (a) Colormap of χ^2 for the $J_1 - J_1' - K$ model with varying J and K terms for $J_1' = 0.75\ J_1$ and comparison to experimental data. (b) Spin-wave calculation for the minimal χ^2 value.

The temperature dependence of the spin-wave excitations in Na_2PrO_3 (with empty cryostat as background subtraction) across the ordering transition at T_N = 4.6 K is shown in Figure S11, revealing a collapse of magnetic excitations above 10 K, corresponding to the gap of ~1 meV in the spectrum.

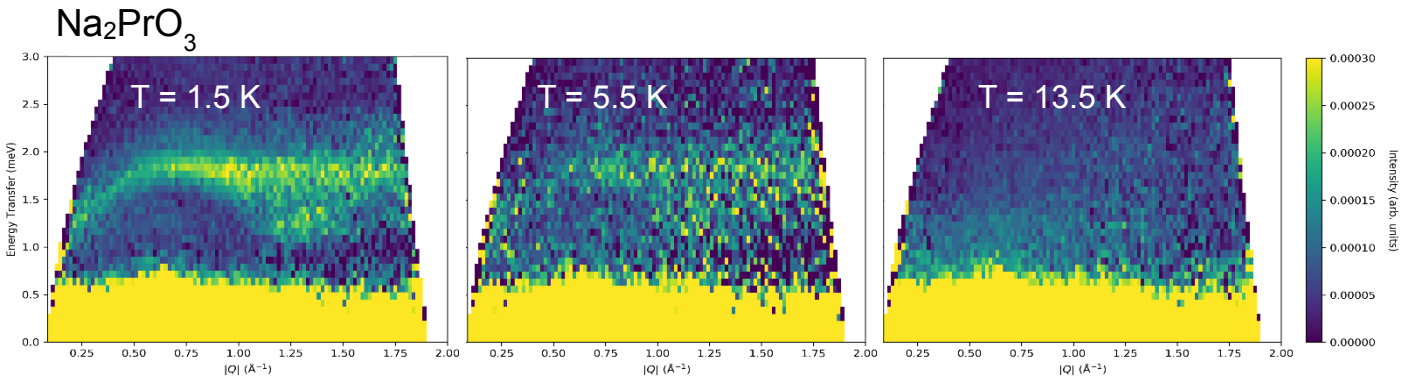

Figure S11. Temperature dependence of Na_2PrO_3 excitation seen with E_i = 8 meV.

Finally, a weak continuum is observed above the noise level in Na_2PrO_3 between 2.0 and 2.3 meV energy transfer which tails to higher energies. This feature is highlighted by the peak asymmetry seen in two constant |Q|-cuts shown in Figure S12 below.

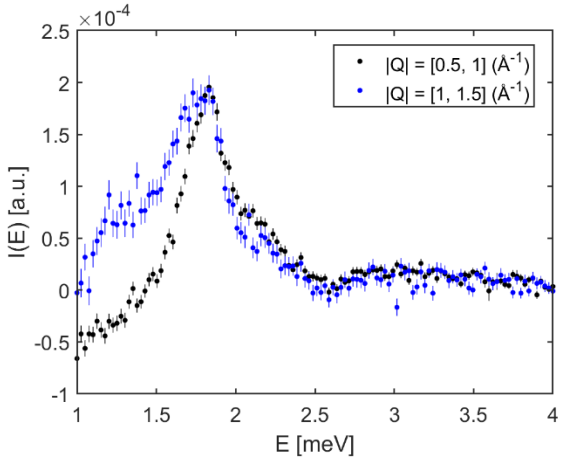

Figure S12. Constant |Q|-cuts of Na_2PrO_3 excitation seen with E_i = 8 meV at T = 1.5 K.

9. Na_2LnO_3 absolute unit normalization and inelastic spectral weight calculations.

Using the method outlined in [16], inelastic neutron scattering results for Na_2TbO_3 with E_i = 20 and 60 meV and Na_2PrO_3 with E_i = 8 meV were converted to absolute units of barns/sr/meV/Ln^{4+} using the FullProf suite. Inelastic spectral weights were calculated by integrating over the entire inelastic signal by utilizing the following two relations [17],

$$\tilde{I}_m(Q,E) = r_0^2 \left|\frac{g}{2}F(Q)\right|^2 2\tilde{S}(Q,E) \qquad (1)$$

$$\mu^2 = 3\mu_B^2 \iint Q^2[g^2\tilde{S}(Q,E)]dQdE / \int Q^2 dQ \qquad (2)$$

where $\tilde{I}_m(Q,E)$ is the measured neutron intensity in absolute units, r_0 = 0.539 x 10^{-12} cm, g is the Landé g-factor, $F(Q)$ is the spherically averaged magnetic form factor for unpaired electrons in the sample, $\tilde{S}(Q,E)$

is the dynamical spin correlation function, and μ^2 is the inelastic spectral weight. These weights are then compared to predicted spectral weights based on magnetic susceptibility from which $\mu_{eff}^2 = g^2 S(S+1)$ is extracted to determine g^2 and subsequently the expected inelastic spectral weight $\mu^2 = g^2 S$. A table of these values can be found below.

Table S4. Summary of inelastic spectral weights for measured neutron scattering data compared to predicted values derived from magnetic susceptibility of Na_2LnO_3 (Ln = Pr^{4+} and Tb^{4+}).

Data Set	**Integrated |Q|-range** ($Å^{-1}$)	μ_{inel}^2 (μ_B^2)
Na_2TbO_3, E_i = 20 meV	[0.48, 2.84]	23.4
Na_2TbO_3, E_i = 60 meV	[0.38, 3.04]	16.2
Na_2TbO_3, susceptibility	N/A	14.51 (2) [expected]
Na_2PrO3, E_i = 8 meV	[0.20, 1.84]	0.3
Na_2PrO_3 susceptibility	N/A	0.6 (2) [expected]

Due to the large experimental uncertainty from the initial normalization to absolute units, instrument broadening of the elastic line, and spherically averaging over a limited number of Brillouin Zones, our results should be understood to have a large systematic uncertainty. In this context, the comparison between the expected and observed inelastic spectral weight for the Tb^{4+} compound at E_i = 20 and 60 meV is decent, see **Table S4**. For Pr^{4+}, E_i = 8 meV, large experimental uncertainty stems from the feed through of the elastic line in the inelastic channel.

10. References.

1. Ramanathan, A.; Leisen, J. E.; La Pierre, H. S., In-Plane Cation Ordering and Sodium Displacements in Layered Honeycomb Oxides with Tetravalent Lanthanides: Na_2LnO_3 (Ln = Ce, Pr, and Tb). *Inorg. Chem.* **2021,** *60* (3), 1398-1410.
2. Loong, C.-K.; Iton, L.; Ozawa, M., Hydrogen vibrational density of states of adsorbed water on rare-earth modified zirconia. *Physica B: Condensed Matter* **1995,** *213*, 640-642.
3. Senesi, R.; Flammini, D.; Kolesnikov, A. I.; Murray, É. D.; Galli, G.; Andreani, C., The quantum nature of the OH stretching mode in ice and water probed by neutron scattering experiments. *The Journal of chemical physics* **2013,** *139* (7), 074504.
4. Granroth, G.; Kolesnikov, A.; Sherline, T.; Clancy, J.; Ross, K.; Ruff, J.; Gaulin, B.; Nagler, S. In *SEQUOIA: A newly operating chopper spectrometer at the SNS*, Journal of Physics-Conference Series, 2010; p 012058.
5. Walter, U., Treating crystal field parameters in lower than cubic symmetries. *J. Phys. Chem. Solids* **1984,** *45* (4), 401-408.
6. Jensen, J.; Mackintosh, A., Rare Earth Magnetism Clarendon Press. Oxford: 1991.
7. Kern, S.; Loong, C.-K.; Lander, G., Crystal-field transitions in *f*-electron oxides. *Phys. Rev. B: Condens. Matter* **1985,** *32* (5), 3051.
8. Boothroyd, A., SPECTRE-a computer program for calculating spectroscopic properties of rare-earth ions in crystals.
9. Wybourne, B., Spectroscopic Properties of Rare Earths (In-terscience, New York, 1965). *The denominator F 2*, 2-1.
10. Kaufman, V.; Sugar, J., The Fifth Spectrum of Praseodymium. *Journal of Research of the National Bureau of Standards. Section A, Physics and Chemistry* **1967,** *71* (6), 583.
11. Hinatsu, Y.; Edelstein, N., Electron paramagnetic resonance spectrum of Pr^{4+} in $BaCeO_3$. *J. Solid State Chem.* **1994,** *112* (1), 53-57.
12. Bleaney, B., Magnetic resonance spectroscopy and hyperfine interactions. *Handbook on the Physics and Chemistry of rare earths* **1988,** *11*, 323-407.
13. Elliott, R. J.; Stevens, K., The theory of magnetic resonance experiments on salts of the rare earths. *Proceedings of the Royal Society of London. Series A. Mathematical and Physical Sciences* **1953,** *218* (1135), 553-566.
14. Rodríguez-Carvajal, J., Recent advances in magnetic structure determination by neutron powder diffraction. *Physica B* **1993,** *192* (1-2), 55-69.
15. Wills, A., A new protocol for the determination of magnetic structures using simulated annealing and representational analysis (SARAh). *Physica B: Condensed Matter* **2000,** *276*, 680-681.
16. Paddison, J.A., Ong, H.S., Hamp, J.O., Mukherjee, P., Bai, X., Tucker, M.G., Butch, N.P., Castelnovo, C., Mourigal, M. and Dutton, S.E., Emergent order in the kagome Ising magnet Dy3Mg2Sb3O14. *Nature communications* **2016**, *7*(1), pp.1-8.
17. Mourigal, M., Fuhrman, W.T., Sheckelton, J.P., Wartelle, A., Rodriguez-Rivera, J.A., Abernathy, D.L., McQueen, T.M. and Broholm, C.L., Molecular quantum magnetism in LiZn 2 Mo 3 O 8. *Physical review letters* **2014**, *112*(2), p.027202.